Reconciling mean-squared radius differences in the silver chain through improved measurement and *ab initio* calculations

B. Ohayon [1,*] J. E. Padilla-Castillo [2] S. C. Wright [2,†] G. Meijer [2] and B. K. Sahoo [3,‡]

[1]*The Helen Diller Quantum Center, Department of Physics, Technion–Israel Institute of Technology, Haifa 3200003, Israel*
[2]*Fritz-Haber-Institut der Max-Planck-Gesellschaft, Faradayweg 4-6, 14195 Berlin, Germany*
[3]*Atomic, Molecular and Optical Physics Division, Physical Research Laboratory, Navrangpura, Ahmedabad 380058, Gujarat, India*

Nuclear charge radius differences in the silver isotopic chain have been reported through different combinations of experiment and theory, exhibiting a tension of two combined standard errors. This study investigates this issue by combining high-accuracy calculations for six low-lying states of atomic silver with an improved measurement of the $5s\,^2S_{1/2} - 5p\,^2P_{3/2}$ transition optical isotope shift. Our calculations predict measured electronic transition energies in Ag I at the 0.3% level, the highest accuracy achieved in this system so far. We calculate electronic isotope shift factors by employing analytical response relativistic coupled-cluster theory and find that a consistent charge radius difference between ^{107,109}Ag is returned when combining our calculations with the available optical isotope shift measurements. We therefore recommend an improved value for the mean-squared charge radius difference between ^{107}Ag and ^{109}Ag as 0.207(6) fm^2, within one combined error from the value derived from muonic Ag experiments, and an updated set of charge radii differences across the isotopic chain.

I. INTRODUCTION

The mean-squared nuclear charge radius difference between isotopes with nuclear mass numbers A and A', $\delta r^2_{A,A'} \equiv r^2_{A'} - r^2_A$, is a unique probe of structural changes in isotopic chains [1], complementary to the binding energy per nucleon. As described in Ref. [2], $\delta r^2_{A,A'}$ values can be inferred from measured isotope shifts (ISs) $\delta \nu_{A,A'} \equiv \nu_{A'} - \nu_A$ using the relation

$$\delta \nu_{A,A'} \simeq K \mu_{A,A'} + F \delta r^2_{A,A'}, \qquad (1)$$

where $\mu_{A,A'} = 1/M_A - 1/M_{A'}$ is the difference between the inverse nuclear masses of isotopes, K denotes the mass shift (MS) factor, and F the field shift (FS) factor of a given transition with frequency ν. The validity and refinements to Eq. (1) are discussed in Sec. II.

When $\delta r^2_{A,A'}$ of two or more isotopic pairs have been measured, usually via muonic atom cascade x-ray spectroscopy [3], the atomic factors K and F of Eq. (1) can be directly extracted from a linear fit called a calibrated King Plot (CKP) [4], having two or more data points. Using this information, $\delta r^2_{A,A'}$ can then be extracted across a chain of isotopes via optical isotope shift measurements, and without further muonic atom experiments. This is the case for most

elements with an even number of protons (Z) [2]. For the odd-Z elements, there are not three or more stable isotopes available that are needed for carrying out traditional cascade spectroscopy measurements (see, however, Refs. [5,6]). So, in order to apply Eq. (1) to extract δr^2 values in a chain of isotopes, one has to rely on the calculation of the IS factors F and K.

For elements in which $\delta r^2_{A,A'}$ for a pair of isotopes has been determined, it is sufficient to calculate or estimate one of the two IS factors, and extract the other factor via Eq. (1). It is convenient to calculate the F values as they are less susceptible to electron correlation effects as compared to K. This method is sometimes referred to as a partial CKP. It is used in odd-Z elements with at least two stable isotopes (see, e.g., [7–9]). It is also useful for light even-Z elements in which a CKP yields larger uncertainties (e.g., [10–14]). The partial CKP method has been considered to give both precise and accurate results for $\delta r^2_{A,A'}$, as it relies on a calculation of F, much easier than of K, and the use of δr^2 from muonic cascade measurements which are considered reliable at a few attometer level. Nevertheless, with tremendous advancement in the development of atomic many-body methods, as well as the availability of ever-increasing computational power, it is possible today to precisely calculate the K values in some systems. This enables the extraction of *all optical* $\delta r^2_{A,A'}$ beyond the accuracy obtained in either a partial or a full CKP approach [15–23], which are forever limited by complex nuclear corrections to the muonic energy levels. A particularly interesting case is that of silver (Ag, $Z = 47$), having two stable isotopes with a similar natural abundance, ^{107}Ag and ^{109}Ag. ISs of three transitions in Ag with unstable nuclei have been measured. In 1975, the $5s\,^2S_{1/2} - 5p\,^2P_{1/2}$ 338 nm and the $5s\,^2S_{1/2} - 5p\,^2P_{3/2}$ 328 nm lines were

*Contact author: bohayon@technion.ac.il
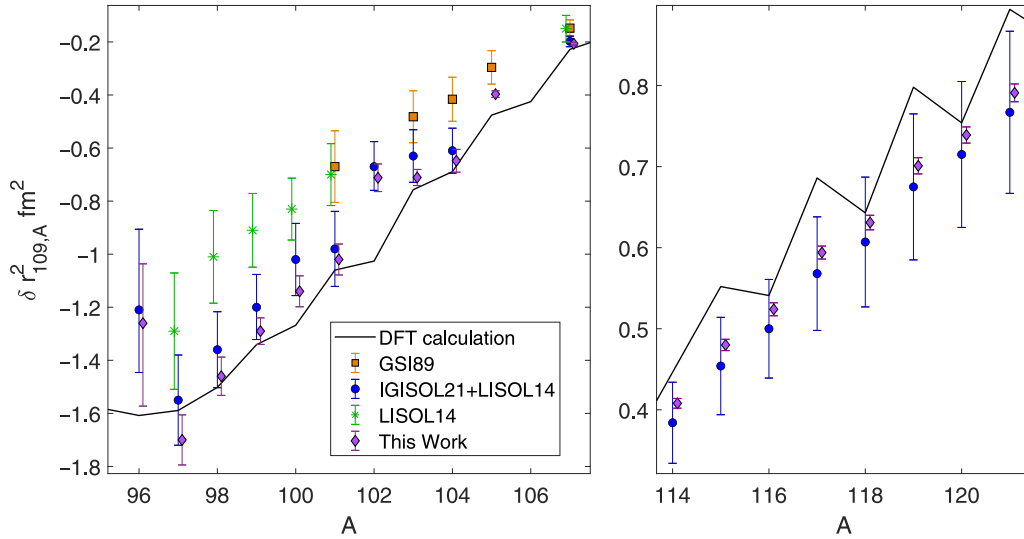†Contact author: sidwright@fhi-berlin.mpg.de
‡Contact author: bijaya@prl.res.in

FIG. 1. Mean-squared charge radius difference, $\delta r^2_{109,A}$, of ground-state silver nuclei as given in Table VI. Error bars show 68% confidence intervals taking into account both statistical and systematic uncertainties. The results of a density-functional-theory (DFT) calculation from Ref. [24] are also shown. The results of this work are in disagreement with the GSI [25] and LISOL [26] measurements and analysis, and agree with recent work in IGISOL [24], though with significantly reduced uncertainties.

measured with a hollow-cathode Fabry-Pérot interferometer using neutron-irradiated targets of ^{108m}Ag and ^{110m}Ag [27]. The first online experiment was performed at the Gesellschaft für Schwerionenforschung (GSI) accelerator facility, where ISs in the $4d^9 5s^2\ ^2D_{5/2} - 6p\ ^2P_{3/2}$ 548 nm line were measured for neutron-deficient isotopes and isomers [25]. Further neutron-deficient isotopes were measured with the 328 nm line at the Leuven Isotope Separator On Line (LISOL) facility [26]. Recently, at the Ion Guide Isotope Separation On-Line (IGISOL) facility, ISs of a long chain of isotopes, extending from ^{96}Ag to ^{121}Ag, were measured, again using the 328 nm line [24]. The center-of-gravity ISs resulting from these efforts have been interpreted via partial CKPs, with different choices for $\delta r^2_{109,107}$ and F, yielding inconsistent results for $\delta r^2_{109,A}$, as shown in Fig. 1.

In this work, we resolve the tension in δr^2 of Ag reported thus far. To do this, we have performed state-of-the-art *ab initio* calculations of IS factors in low-lying levels of Ag I. Our results indicate that semiempirical estimations of K and F, used in previous studies of Ag, deviate by two combined standard errors. We also provide an improved optical isotope shift of the 328 nm transition in naturally abundant Ag, and perform a global analysis of the result with the available literature data. Our calculations of K and F for these transitions in Ag, combined with the data, produce a consistent value for $\delta r^2_{109,107}$ within a few percent. This checks the consistency of our calculations.

Having validated our calculation, we use the available optical IS data to provide $\delta r^2_{109,A}$ for the silver isotope chain spanning $A = 96$–105, $A = 114$–121, and six long-lived isomers. These results reduce the uncertainty in $\delta r^2_{109,A}$ by up to a factor of seven. A comparison with prior works pinpoints the reasons for past inconsistencies. Finally, the recommended $\delta r^2_{109,A}$ of the Ag isotopes are compared with state-of-the-art nuclear theory calculations. While the overall trend of the nuclear calculations agrees with the data extracted by

combining our atomic calculations with the IS measurements, a few interesting deviations are noticed.

II. VALIDITY OF LINEAR APPROXIMATION

Before calculating the IS factors, we discuss refinements to Eq. (1), in light of our aim of extracting δr^2 in a long chain of isotopes, in which the charge radius is expected to vary significantly. As seen in Fig. 1, the isotopic difference in the mean-squared radius can be as large as 2.6 fm^2, so that the root-mean-squared radii span the range $R = 4.37$–4.64 fm. In this work, we take into account a possible dependency of K and F on R by repeating their calculation for different values of R in a range larger than that spanned by the experimental values.

Another refinement of Eq. (1) is due to variation of the nuclear shape among the isotopes. The effect on the IS can be estimated via a change to the FS factor, $\delta F_{A,A'} = C(rcc^4_{A'}/r^2_{A'} - rcc^4_A/r^2_A)$, with rcc the fourth radial moment and $C \simeq -6 \times 10^{-4}$ fm^{-2} the Seltzer coefficient calculated in [28]. As the ratio of moments depends on the nuclear shape, we estimate their maximal change by varying the skin thickness parameter by 10% in Eq. (3), as suggested in Ref. [2]. It shows a 2% variation in $\delta F_{A,A'}$, which is in agreement with the finding of Ref. [25] [see their Eq. (20)] that was also adopted in Ref. [24]. To be more conservative, and following the discussion given in Ref. [20], we treat this contribution not as a correction, but as another source of uncorrelated uncertainty to the nuclear radii extraction in the Ag isotopes.

It is also worth noting that in this work, ISs are defined as the centers of gravity of the hyperfine manifold. When there are nearby states of equal parity, the mixing of fine and hyperfine structures introduces a nuclear spin-dependent shift of the ISs (see, e.g., [29]). For the energy levels of Ag that are of interest to this work, the largest shift would be due to the mixing of fine and hyperfine structures in the $5p$

manifold. The order of magnitude of this shift can be roughly estimated by $\Delta E^{(2)} \simeq A(5p\ ^2P_{1/2})A(5p\ ^2P_{3/2})/\Delta E_{FS}$ [30,31], where $\Delta E_{FS} = 28$ THz is the fine structure of the $5p$ manifold. Even for the isotopes with the largest magnetic moments, $\Delta E^{(2)} \simeq 10$ kHz. It is three orders smaller than the precision of interest to the present work, and hence it can be safely neglected.

III. ATOMIC CALCULATIONS

A. Method of calculation

We consider the Dirac-Coulomb (DC) Hamiltonian to calculate the IS factors in the relativistic framework, given in

atomic units (a.u.) by

$$H = \sum_i \left[c\vec{\alpha}_i^D \cdot \vec{p}_i + (\beta_i^D - 1)c^2 + V_n(r_i) \right] + \sum_{i,j>i} \frac{1}{r_{ij}}, \quad (2)$$

where c is the speed of light, $\vec{\alpha}^D$ and β^D are the Dirac matrices, $\vec{p}$ is the single-particle momentum operator, $V_n(r)$ denotes the nuclear potential seen by an electron at distance r from the nucleus, and $\frac{1}{r_{ij}}$ represents the Coulomb potential between the electrons located at the ith and jth positions. The finite size of the nucleus is defined by a two-parameter Fermi-charge distribution, given by

$$\rho(r) = \frac{\rho_0}{1 + e^{(r-b)/a}}, \quad (3)$$

where ρ_0 is the normalization constant, b is the half-charge radius, and $a = 2.3/4\ln(3)$ is an approximate skin thickness. It yields

$$V_n(r) = -\frac{Z}{\mathcal{N}r} \begin{cases} \frac{1}{b}\left[\frac{3}{2} + \frac{a^2\pi^2}{2b^2} - \frac{r^2}{2b^2} + \frac{3a^2}{b^2}P_2^+ \frac{6a^3}{b^2r}(S_3 - P_3^+)\right] & \text{for } r_i \leqslant b \\ \frac{1}{r_i}\left[1 + \frac{a62\pi^2}{b^2} - \frac{3a^2r}{c^3}P_2^- + \frac{6a^3}{b^3}(S_3 - P_3^-)\right] & \text{for } r_i > b, \end{cases} \quad (4)$$

where the factors are

$$\mathcal{N} = 1 + \frac{a^2\pi^2}{b^2} + \frac{6a^3}{b^3}S_3,$$

$$\text{with} \quad S_k = \sum_{l=1}^{\infty} \frac{(-1)^{l-1}}{l^k}e^{-lb/a}$$

$$\text{and} \quad P_k^\pm = \sum_{l=1}^{\infty} \frac{(-1)^{l-1}}{l^k}e^{\pm l(r-b)/a}. \quad (5)$$

In the above expression, b is obtained using the relation

$$b \simeq \sqrt{\frac{5}{3}R^2 - \frac{7}{3}a^2\pi^2}, \quad (6)$$

where R is the approximate root-mean-squared radius and calculated from the empirical relation [37]

$$R \simeq (0.836A^{1/3} + 0.57) \text{ fm}. \quad (7)$$

We later show that the excitation energies and IS factors very weakly depend on the assumed value of the charge radius, thus validating the above approximations. The FS operator F is defined in this case as

$$\hat{F} = -\frac{\delta V_n(r)}{\delta R} = -\frac{\partial V_n(r)}{\partial b}\frac{\delta b}{\delta R}. \quad (8)$$

In the relativistic formulation, the normal mass shift (NMS) and specific mass shift (SMS) operators are given by

$$O^{NMS} = \frac{1}{2}\sum_i \left[\vec{p}_i^2 - \frac{\alpha_e Z}{r_i}\vec{\alpha}_i^D \cdot \vec{p}_i - \frac{\alpha_e Z}{r_i}(\vec{\alpha}_i^D \cdot \vec{C}_i^1)\vec{C}_i^1 \cdot \vec{p}_i \right] \quad (9)$$

and

$$O^{SMS} = \frac{1}{2}\sum_{i\neq j} \left[\vec{p}_i \cdot \vec{p}_j - \frac{\alpha_e Z}{r_i}\vec{\alpha}_i^D \cdot \vec{p}_j \right.$$
$$\left. - \frac{\alpha_e Z}{r_i}(\vec{\alpha}_i^D \cdot \vec{C}_i^1)(\vec{p}_j \cdot \vec{C}_j^1) \right], \quad (10)$$

respectively, where α_e is the fine-structure constant and $\vec{C}$ is the Racah angular momentum operator. Contributions from the Breit and lower-order QED interactions are also estimated, by including them self-consistently in the calculations [38], as corrections to the DC Hamiltonian results.

Expectation values of F, O^{NMS}, and O^{NMS} with respect to the wave function of an atomic state will correspond to the FS, NMS, and SMS factors, respectively. It should be noted from Eq. (7) that different R values can affect $V_n(r)$ and, hence, calculation of the atomic wave functions. We later validate that such changes in wave functions do not affect the energies, NMS factors, and SMS factors at the precision of our interest, but it may affect calculations of the FS factors as the F operator can have nonlinear dependency on R. We demonstrate this dependency by calculating the energies and IS factors later with different values of R.

The Ag atom has the ground-state configuration $[4d^{10}]5s$. Our interest is to calculate the difference in the values between two states of the IS factors of the $5s\ ^2S_{1/2} - 5p\ ^2P_{1/2;3/2}$, $5s\ ^2S_{1/2} - 6s\ ^2S_{1/2}$, and $5s\ ^2S_{1/2} - 6p\ ^2P_{1/2;3/2}$ transitions in this work. We calculate these factors for each state using the relativistic coupled-cluster (RCC) theory by adopting the analytical-response approach (AR-RCC method) as described in Ref. [15]. It requires the determination of wave functions of the ground state as well as for the $5p\ ^2P_{1/2;3/2}$, $6s\ ^2S_{1/2}$, and $6p\ ^2P_{1/2;3/2}$ states of Ag I. To conveniently obtain all these states, we first calculate the wave function ($|\Psi_0\rangle$) of the common closed-shell core configuration $[4d^{10}]$ of all these states by expressing it in the RCC theory ansatz [39],

$$|\Psi_0\rangle = e^{S_0}|\Phi_0\rangle, \quad (11)$$

where S_0 is the RCC excitation operator carrying electron correlation effects and the reference state $|\Phi_0\rangle$ is the mean-field wave function of the closed-shell $[4d^{10}]$ configuration, obtained in the Dirac-Hartree-Fock (DHF) method. The

amplitude determining the equation for S_0 is given by

$$\langle \Phi_0^* | (He^{S_0})_l | \Phi_0 \rangle = 0, \qquad (12)$$

where $|\Phi_0^*\rangle$ represents all possible excited-state determinants with respect to $|\Phi_0\rangle$ and subscript l means linked terms. First, we approximate the RCC theory at the singles and doubles approximation (RCCSD method), in which the S_0 is defined as

$$S_0 = S_{10} + S_{20} = \sum_{a,p} s_{ap} a_p^\dagger a_a + \frac{1}{4} \sum_{a,b,p,q} s_{ap,bq} a_p^\dagger a_q^\dagger a_b a_a, \qquad (13)$$

where S_{10} and S_{20} stand for single and double excitations of the RCC operator S_0 with the amplitudes s_{ap} and $s_{ap,bq}$, respectively. Here, a, b denote occupied orbitals and p, q represent unoccupied (virtual) orbitals. Following Eq. (12), it yields

$$s_{ap} = \frac{\langle \Phi_a^p | H + [(He^{S_0})_l - H]]_{\text{ofd}} | \Phi_0 \rangle}{\epsilon_a - \epsilon_p}$$

and

$$s_{ap,bq} = \frac{\langle \Phi_{ab}^{pq} | H + [(He^{S_0})_l - H]]_{\text{ofd}} | \Phi_0 \rangle}{\epsilon_a + \epsilon_b - \epsilon_p - \epsilon_q}, \qquad (14)$$

where $|\Phi_0^*\rangle$ are taken as $|\Phi_a^p\rangle = a_p^\dagger a_a |\Phi_0\rangle$ and $|\Phi_{ab}^{pq}\rangle = a_p^\dagger a_q^\dagger a_b a_a |\Phi_0\rangle$ representing the singly and doubly excited Slater determinants, respectively. Here the subscript ofd denotes off-diagonal terms and ϵ's are the single-particle orbital energies.

After obtaining the solution for $|\Psi_0\rangle$, we determine the wave function of an atomic state ($|\Psi_v\rangle$) of Ag I with a valence orbital v by defining [40,41]

$$|\Psi_v\rangle = e^{S_0 + S_v} |\Phi_v\rangle = e^{S_0} \{1 + S_v\} |\Phi_v\rangle, \qquad (15)$$

where $|\Phi_v\rangle = a_v^\dagger |\Phi_0\rangle$ is the modified DHF wave function, and S_v includes excitation configurations due to correlation effects by the valence electron. In the RCCSD method, we define

$$S_v = S_{1v} + S_{2v} = \sum_{p \neq v} s_{vp} a_p^\dagger a_v + \frac{1}{2} \sum_{p \neq v,b,q} s_{vp,bq} a_p^\dagger a_q^\dagger a_b a_v, \qquad (16)$$

where S_{1v} and S_{2v} stand for single and double excitations of the RCC operator S_v with the amplitudes s_{vp} and $s_{vp,bq}$, respectively. Like the case for the S_0 operator, amplitudes of the S_v operator are determined by

$$\langle \Phi_v^* | \{(He^{S_0})_l - E_v\} S_v + (He^{S_0})_l | \Phi_v \rangle = 0, \qquad (17)$$

where $|\Phi_v^*\rangle$ denotes singly and doubly excited Slater determinants with respect to $|\Phi_v\rangle$. It corresponds to

$$s_{vp} = \frac{\langle \Phi_v^p | (He^{S_0})_l + [(He^{S_0})_l S_v]_{\text{ofd}} | \Phi_v \rangle}{E_v - \epsilon_p}$$

and

$$s_{vp,bq} = \frac{\langle \Phi_{vb}^{pq} | (He^{S_0})_l + [(He^{S_0})_l S_v]_{\text{ofd}} | \Phi_v \rangle}{E_v + \epsilon_b - \epsilon_p - \epsilon_q}. \qquad (18)$$

The energy of the respective state is given by

$$E_v = \langle \Phi_v | (He^{S_0})_l \{1 + S_v\} | \Phi_v \rangle. \qquad (19)$$

Both Eqs. (17) and (19) are solved simultaneously by adopting a self-consistent procedure. Here we use a normal-ordered Hamiltonian with respect to $|\Phi_0\rangle$, so that the calculated E_v value will correspond to the electron affinity (EA) rather than the total energy of $|\Psi_v\rangle$. Excitation energy (EE) of a transition can be obtained from the difference between the EAs of two states associated with the transition.

In the AR-RCC method, we estimate IS factors as the first-order energy correction to the calculated E_v value of the state $|\Psi_v\rangle$ due to the corresponding IS operator (denoted by H_{IS} in general). Hereafter, we identify the RCC operators and calculated energies due to the DC Hamiltonian with superscript (0) and the first-order corrections in the AR-RCC method are denoted by the superscript (1) as described in Ref. [15]. In the AR-RCC method, the first-order energy correction ($E_v^{(1)}$) is obtained as the solution of the following equation:

$$\left(H - E_v^{(0)}\right)\left|\Psi_v^{(1)}\right\rangle = \left(E_v^{(1)} - H_{\text{IS}}\right)\left|\Psi_v^{(0)}\right\rangle. \qquad (20)$$

In the singles and doubles excitation approximation of the AR-RCC approach (AR-RCCSD method), the amplitudes of the $S_0^{(1)}$ and $S_v^{(1)}$ operators are defined in the similar way as in the case of unperturbed case and they are obtained by

$$\langle \Phi_0^* | \left(He^{S_0^{(0)}} S_0^{(1)} + H_{\text{IS}} e^{S_0^{(0)}}\right)_l | \Phi_0 \rangle = 0 \qquad (21)$$

and

$$\begin{aligned} \langle \Phi_v^* | \{ &\left(He^{S_0^{(0)}}\right)_l - E_v^{(0)}\} S_v^{(1)} + \left(He^{S_0^{(0)}} S_0^{(1)}\right)_l \\ &\times \{1 + S_v^{(0)}\} + \left(H_{\text{IS}} e^{S_0^{(0)}}\right)_l \{1 + S_v^{(0)}\} \\ &+ E_v^{(1)} S_v^{(0)} | \Phi_v \rangle = 0. \end{aligned} \qquad (22)$$

In the above equation, the expression for an IS factor is given by

$$\begin{aligned} E_v^{(1)} = \langle \Phi_v | &\left(He^{S_0^{(0)}}\right)_l S_v^{(1)} + \left(He^{S_0^{(0)}} S_0^{(1)}\right)_l \{1 + S_v^{(0)}\} \\ &+ \left(H_{\text{IS}} e^{S_0^{(0)}}\right)_l \{1 + S_v^{(0)}\} | \Phi_v \rangle. \end{aligned} \qquad (23)$$

It should be noted that Eqs. (21), (22), and (23) are the first-order approximations of Eqs. (12), (17), and (19), respectively. Therefore, the amplitudes of the perturbed operators of the AR-RCC method follow similar expressions corresponding to their respective unperturbed RCC operators.

In this work, we considered correlations from electrons among the $20s$, $20p$, $19d$, $18f$, $16g$, $14h$, and $12i$ orbitals. Since considering triple excitations among all these orbitals was not feasible with the available computational resources, we have allowed triple excitations up to $15s$, $15p$, $15d$, $11f$, and $10g$ orbitals along with the correlations from the RCCSD method. It should be noted that we have not counted spin multiplicity of the orbitals here.

To demonstrate contributions to the IS factors at different levels of approximations in the atomic Hamiltonian, we give results using the DC Hamiltonian and corrections due to the Breit (given as +Breit) and QED (given as +QED) effects at the RCCSD method. Differences of the RCCSD values from the larger basis set are given as "+Basis" contribution. Estimated contributions from the triple excitations are listed as "+T." We also present calculated energies at the second perturbation theory (MP2 method) using the $20s$, $20p$, $19d$,

TABLE I. Comparison of calculated and measured energies. Calculated electron affinities (EAs, where zero energy refers to the ground state of Ag II) of the considered states in Ag at different levels of approximation. The estimated excitation energies (EEs) are also quoted. Unless otherwise stated, all values are in cm^{-1}. Our final results are compared with the experimental values (denoted Expt.). Differences between our calculated and experimental values are shown as Δ in percentage. The last column gives the results of prior calculations available in the literature which are closest to experiment.

State	DHF	MP2	RCCSD	+T	+Basis	+Breit	+QED	Total	Expt. [32,33]	$\Delta\%$	Lit.
EAs											
$5s\ ^2S_{1/2}$	50376	61014	60408	441(110)	193(96)	-59	$-22(22)$	60961(148)	61106.5(2)	0.2(2)	60823 [34]
$5p\ ^2P_{1/2}$	26730	30771	31007	455(114)	46(23)	-36	4(4)	31477(116)	31554.4(2)	0.2(4)	31066 [34]
$5p\ ^2P_{3/2}$	26148	29862	30089	442(111)	39(20)	-24	$-4(4)$	30543(112)	30633.7(2)	0.3(4)	30184 [34]
$6s\ ^2S_{1/2}$	17115	18641	18455	45(11)	21(11)	-8	$-3(3)$	18510(16)	18550.3(2)	0.2(1)	18494 [34]
$6p\ ^2P_{1/2}$	11786	12726	12680	89(22)	9(5)	-8	1(1)	12771(23)	12809.0(2)	0.3(2)	12656 [35]
$6p\ ^2P_{3/2}$	11618	12502	12467	94(24)	8(4)	-5	$-1(1)$	12563(24)	12606.6(2)	0.3(2)	12452 [35]
EEs											
$5s\ ^2S_{1/2}-5p\ ^2P_{1/2}$	23646	30243	29400	$-14(4)$	147(73)	-24	$-25(25)$	29484(78)	29552.061(1)	0.2(3)	29496 [35]
$5s\ ^2S_{1/2}-5p\ ^2P_{3/2}$	24228	31152	30319	$-2(0.)$	154(77)	-36	$-18(18)$	30418(79)	30472.703(1)	0.2(3)	30451 [36]
$5s\ ^2S_{1/2}-6s\ ^2S_{1/2}$	33261	42373	41953	396(99)	172(86)	-51	$-19(19)$	42451(105)	42556.152(2)	0.2(3)	42329 [34]
$5s\ ^2S_{1/2}-6p\ ^2P_{1/2}$	38590	48288	47727	352(88)	185(92)	-51	$-23(23)$	48190(108)	48297.402(3)	0.2(3)	47765 [35]
$5s\ ^2S_{1/2}-6p\ ^2P_{3/2}$	38758	48512	47940	347(87)	185(93)	-54	$-21(21)$	48398(103)	48500.805(2)	0.2(3)	47969 [35]

$18f$, and $16g$ orbitals to demonstrate the importance of considering an all-order method such as RCC theory for accurate calculations of the properties in Ag. Most of the uncertainty in our calculated energies and IS factors would stem from the frozen orbitals in the estimations of the triples contributions. High-lying orbitals that are not included in the RCCSD calculations can also contribute, to some extent, to the IS factors. We have accounted for possible uncertainties from these contributions after estimating them in the MP2 method.

B. Results and discussion

1. Energies

In Table I, we give results for the calculated EAs. They are given first at the DHF approximation, which already captures the gross level structure. When taking into account electron correlations through either MP2 or RCCSD, the EAs of the $n = 5$ manifold increase by $O(15\%)$. The effect is stronger than in the isoelectronic Cd II, where it is 8–9%, indicating that electron correlations are more important in Ag I. For the $n = 6$ manifold, the increase is half the size, hinting that correlations in more weakly bound single-valence states play smaller roles, as expected. Introducing correlation effects through triple excitations increases the EAs of the $n = 5$ manifold by 0.7–1.5%, twice as much as in Cd II, and three times that for the $n = 6$ manifold. The uncertainty tied to missing quadruple electron excitation contributions to EAs is expected to be small. The basis set extrapolation increases the EAs for all levels as well.

The Breit and QED contributions are found to be small, but not negligible. We find that for states with ns valence orbitals, the Breit and QED corrections are comparable in magnitude, while for states with the np subshells, the former is much larger, as was pointed out in [42]. Our approximate QED correction to the $5s\ ^2S_{1/2}$ EA is found to be smaller than most other literature values, as compiled in Table VIII of [42]. For this reason, we ascribe a 100% uncertainty to it and to the corresponding corrections to the IS operators.

Although these uncertainties are negligible with respect to other contributions, they point out that moving to heavier or multiply charged systems without losing accuracy would necessitate a refinement of the QED treatment.

The total EAs are 0.2–0.3% away from experiment, within two standard deviations from our estimated uncertainty. They are closer to the experimental values than the closest results from the literature [34,35], which do not quote uncertainties, by up to a factor of 8. Due to the stronger electron correlations, the total uncertainty is a factor of 2–3 higher than in our prior work on Cd II. All in all, we undershoot the experimental energies, which indicates that a more complete treatment of electron correlations is necessary for accurate estimations of the results. For Cd II, we overshot the experimental energies, indicating possibly underestimated many-body QED effects.

The EEs are calculated from the differences of the other level EAs to that of the $5s\ ^2S_{1/2}$ ground level at different approximations. Similarly to the EAs, the EEs are 0.2% away from experimental measurements, within our uncertainty estimation. The EEs of the $n = 5$ doublet are less accurate than in the prior works [35,36], while those of the higher states are more so [34,35]. It is interesting to note that contributions from the triple excitations are similar for each state in the manifold. This means that the uncertainty is dominated by basis extrapolation for the first two EEs.

2. IS factors

In Table II, we give the IS factors evaluated at different levels of approximation. We first discuss the FS factors from our calculations. At the DHF level, $F(5s\ ^2S_{1/2})$ and $F(6s\ ^2S_{1/2})$ are large stemming from strong overlap with the nucleus, $F(5p\ ^2P_{1/2})$ and $F(6p\ ^2P_{1/2})$ are small but nonnegligible, and $F(5p\ ^2P_{3/2})$ and $F(6p\ ^2P_{3/2})$ are negligible. Our result for $F_{328} \equiv F(5p\ ^2P_{3/2}) - F(5s\ ^2S_{1/2})$ is close to the Hartree-Fock calculation in [25], but differs from their Dirac-Fock calculation. Introducing electron correlations at the AR-RCCSD approximation increases $F(5s\ ^2S_{1/2})$ by

TABLE II. Calculated isotope shift factors F, K^{SMS}, and K^{NMS} for selected levels in Ag I. For each of the calculated values, we first list factors relative to the ground state of the Ag II ion, followed by factors for optical transitions from the $5s\,^2S_{1/2}$ ground state of Ag I. F and K^{SMS} are compared with semi-empirical values from the literature, while K^{NMS} is compared with the values returned from the scaling law (SL), as discussed in the main text. Calculations are performed with $R = 4.55$ fm; the effect of repeating them with different radii is shown in Table III.

State	DHF	AR-RCCSD	+T	+Basis	+Breit	+QED	Total	
F MHz/fm^2								
$5s\,^2S_{1/2}$	−2527	−3852	129(32)	−30(15)	11	19(19)	−3723(40)	
$5p\,^2P_{1/2}$	−17	−163	−37(9)	1(1)	1	1(1)	−197(9)	
$5p\,^2P_{3/2}$	−0.	−126	−42(11)	2(1)	1	1(1)	−165(11)	
$6s\,^2S_{1/2}$	−412	−517	15(4)	−1(1)	1	2(1)	−499(5)	
$6p\,^2P_{1/2}$	−5	−32	−11(3)	1(0.)	0.	0.(0.)	−42(3)	
$6p\,^2P_{3/2}$	−0.	−25	−15(4)	1(0.)	0.	0.(0.)	−39(4)	
$5s\,^2S_{1/2}-5p\,^2P_{1/2}$	−2510	−3689	166(42)	−31(15)	10	19(19)	−3525(48)	
$5s\,^2S_{1/2}-5p\,^2P_{3/2}$	−2527	−3726	171(43)	−31(16)	10	18(18)	−3557(49)	
Ref. [25]	−2625, −3146						−4265(341)	
Refs. [24,26]							−4300(300)	
$5s\,^2S_{1/2}-6s\,^2S_{1/2}$	−2115	−3336	114(29)	−28(14)	10	17(17)	−3223(36)	
$5s\,^2S_{1/2}-6p\,^2P_{1/2}$	−2522	−3820	141(35)	−30(15)	11	19(19)	−3680(43)	
$5s\,^2S_{1/2}-6p\,^2P_{3/2}$	−2527	−3827	144(36)	−30(15)	11	19(19)	−3683(43)	
K^{SMS} GHz u								
$5s\,^2S_{1/2}$	−1611	1346	115(29)	−4(2)	5	1(1)	1463(29)	
$5p\,^2P_{1/2}$	−553	342	68(17)	−3(2)	−1	−0.(0.)	405(17)	
$5p\,^2P_{3/2}$	−464	370	64(16)	−3(1)	−0.	−0.(0.)	432(16)	
$6s\,^2S_{1/2}$	−253	176	28(7)	−2(1)	1	0.(0.)	202(7)	
$6p\,^2P_{1/2}$	−150	65	23(6)	−1(1)	0.	−0.(0.)	88(6)	
$6p\,^2P_{3/2}$	−128	75	25(6)	−1(0.)	0.	−0.(0.)	99(6)	
$5s\,^2S_{1/2}-5p\,^2P_{1/2}$	−1058	1005	47(12)	−1(0.)	6	1(1)	1058(12)	
$5s\,^2S_{1/2}-5p\,^2P_{3/2}$	−1146	976	51(13)	−1(1)	5	1(1)	1031(13)	
Ref. [26]							150(450)	
$5s\,^2S_{1/2}-6s\,^2S_{1/2}$	−1358	1171	87(22)	−2(1)	4	0.(0.)	1260(22)	
$5s\,^2S_{1/2}-6p\,^2P_{1/2}$	−1461	1281	92(23)	−3(1)	5	1(1)	1375(23)	
$5s\,^2S_{1/2}-6p\,^2P_{3/2}$	−1482	1271	90(23)	−3(2)	5	1(1)	1363(23)	
K^{NMS} GHz u								SL
$5s\,^2S_{1/2}$	3393	808	36(9)	11(5)	−1	−1(1)	852(11)	1005
$5p\,^2P_{1/2}$	1200	367	51(13)	5(3)	−1	0.(0.)	422(13)	519
$5p\,^2P_{3/2}$	1111	351	49(12)	5(3)	−1	−0.(0.)	405(13)	504
$6s\,^2S_{1/2}$	667	274	2(1)	1(1)	−0.	−0.(0.)	277(1)	305
$6p\,^2P_{1/2}$	396	181	5(1)	1(1)	−0.	0.(0.)	187(1)	211
$6p\,^2P_{3/2}$	376	176	5(1)	1(1)	−0.	−0.(0.)	182(1)	207
$5s\,^2S_{1/2}-5p\,^2P_{1/2}$	2193	441	−14(4)	5(3)	−0.	−1(1)	431(5)	486
$5s\,^2S_{1/2}-5p\,^2P_{3/2}$	2282	457	−13(3)	5(3)	−1	−1(1)	448(4)	501
$5s\,^2S_{1/2}-6s\,^2S_{1/2}$	2727	534	34(9)	9(5)	−1	−1(1)	575(10)	700
$5s\,^2S_{1/2}-6p\,^2P_{1/2}$	2998	627	31(8)	9(5)	−1	−1(1)	665(9)	764
$5s\,^2S_{1/2}-6p\,^2P_{3/2}$	3017	632	32(8)	9(5)	−1	−1(1)	671(9)	798

50%, and $F(6s\,^2S_{1/2})$ by 25%. This trend is similar to that seen with the EAs. Correlations also increase F of the nP levels, thus reducing the magnitudes for the fine-structure intervals. Triple excitation contributions to $F(5s\,^2S_{1/2})$ reduce its magnitude by 3%, twice as much and of opposite sign as in Cd II. In Zn II, triple contributions to $F(4s\,^2S_{1/2})$ are of the same sign and five times smaller then in Ag I [20]. These observations demonstrate the nontrivial nature of correlation effects from the high-level excitations, and motivate extending these calculations to the homologous levels in Cu I in order to gain further insight. As in Cd II and Zn II, the contribution of approximate QED corrections is much larger than that of the

Breit interaction. Nevertheless, it is still small compared with our uncertainty estimation.

Note that ours is an *ab initio* calculation of the FS factor in Ag I levels. Nevertheless, it was semi-empirically extracted from the $5s\,^2S_{1/2}$ hyperfine structure, yielding $F_{328,SE} = -4265(341)$ MHz/fm^2, with SE shorthand for semi-empirical, given in [25]. A similar estimation was also used in recent works [24,26]. $F_{328,SE}$ is larger than our recommended value by two of its standard deviations. A quarter of the difference is directly related to the missing contribution from the $5p$ level, and another quarter from their estimation of the higher-moment contribution. These

observations support other studies (see [12,43,44]) which suggest that semi-empirically estimated values of F are about 20% too large. While this effect was already reported by Torbohm *et al.* in 1985 [45], semi-empirical values for F are still often assigned a much smaller error in the literature.

The SMS factor K^{SMS}, tied to a two-body operator, is entirely affected by electron correlations; so much so that its calculated value is meaningless at the mean-field approximation. At the AR-RCCSD approximation, $K^{\mathrm{SMS}}(5s\ ^2S_{1/2})$ is of similar magnitude in Ag I and Cd II. However, $K^{\mathrm{SMS}}(5p)$ for both levels of the doublet is 2.5 times larger in Ag. Triple excitation contributions are twice larger for $K^{\mathrm{SMS}}(5s\ ^2S_{1/2})$ and an order of magnitude larger for both $K^{\mathrm{SMS}}(5p\ ^2P_{1/2})$ and $K^{\mathrm{SMS}}(5p\ ^2P_{3/2})$ Surprisingly, K^{SMS} converges fast with increasing basis size. This is fortunate as the calculation of K^{SMS} at the AR-CC singles doubles triples (AR-CCSDT) approximation already requires several months of computation time on a medium-sized high-performance cluster. As in Cd II, the Breit and QED corrections to K^{SMS} are completely negligible. Thus, the total uncertainty is dominated by our estimation of contributions from the missing quadruple excitations.

To our knowledge, there are no available *ab initio* calculations of K^{SMS} to be compared with. Nevertheless, we can test the heuristic used in [26], that $K_{\mathrm{SE}}^{\mathrm{SMS}} \approx 0.3(9)K_{\mathrm{SL}}^{\mathrm{NMS}} = 150(450)\,\mathrm{GHz\,u}$, where the NMS factor was estimated through the scaling law (SL) $K_{\mathrm{SL}}^{\mathrm{NMS}} = -m_e\Delta E = 501\,\mathrm{GHz\,u}$, with ΔE the measured energy difference. Even though a large uncertainty is attached to this semi-empirical calculation, our result lies two standard deviations away, putting some doubts on the reliability of using this semi-empirical method.

Although K^{NMS} is estimated from a one-body operator, it is highly affected by electron correlations, with the AR-CCSD value only a third of the DHF value. Triple excitations contribute around 10% to the $n=5$ manifold states, as seen in Cd II. For the $n=6$ manifold, the effect of correlations is smaller: half and a few percent in the AR-RCCSD method and after including contributions from the triple excitations, respectively. Breit contributions to K^{NMS} are found to be small but not negligible, while QED contributions are negligible. A difference of 10 to 20% between the calculated K^{NMS} and the one semi-empirically estimated via scaling law is observed for all levels. It is much larger than the difference seen in Cd II, indicating that its origin is from electron correlations, stronger in Ag I, than from the relativistic effects, stronger in Cd II. A discussion on this phenomenon can be found in Ref. [46].

The calculations are repeated for different values of R in a range spanning the root-mean-squared radii of ^{96}Ag$-^{121}$Ag. The results are given in Table III and show that the dependency of the calculated IS factors on R is negligible compared with our reported uncertainties. Nevertheless, we take them into account when extracting δr^2 away from stability.

IV. MEASUREMENTS ON THE $5s\ ^2S_{1/2} \rightarrow 5p\ ^2P_{3/2}$ LINE AT 328 NM

To improve the available measurements for the naturally occurring isotopes of Ag, we perform continuous-wave laser-induced fluorescence spectroscopy with a buffer gas cooled atomic beam. The spectrometer used for these measurements

has been previously described [47–49]. Briefly, Ag atoms of natural isotopic abundance (52% ^{107}Ag and 48% ^{109}Ag) are produced by laser ablation inside a cryogenically cooled copper cell, thermalized by colliding with a He buffer gas at a temperature of 3 K, and exit the cell as a slow, pulsed atomic beam. At a distance of 70 cm from the exit of the buffer gas cell, the atoms interact with a low-intensity probe laser beam which excites the $5s\ ^2S_{1/2} \rightarrow 5p\ ^2P_{3/2}$ transition near 328 nm. The laser light is produced by frequency doubling a narrow-linewidth ring dye laser (Sirah Matisse 2DX) at 656 nm. The frequency of the 656 nm light is recorded using a commercial wave meter (High Finesse WS8-10, calibrated with a temperature stabilized HeNe laser), which provides an absolute accuracy of 20 MHz at 328 nm. Laser-induced fluorescence is collected using a photomultiplier tube whose photocurrent is delivered to a transimpedance amplifier to generate a time-of-flight trace. Based on the range of arrival times at the detector, we estimate that the range of velocities in the beam covers 90 to 130 m/s (full width at half maximum). The transverse velocity width of the atomic beam is restricted using a 2 mm square aperture mounted immediately in front of the detector. Orthogonality with the atomic beam direction is ensured using a set of alignment irises mounted on the detection vacuum chamber; we additionally verify and limit residual Doppler shifts due to misalignment by comparing spectra by arrival time at the detector, as discussed later.

Figure 2(a) shows the relevant energy levels for ^{107,109}Ag, both of which have a nuclear spin of $I = 1/2$. Levels within the ground (excited) levels are labeled by their hyperfine angular momentum quantum number F (F'), and the optical transitions are labeled by their respective line intensities. In the experiment, the hyperfine structure in the $^2S_{1/2}$ and $^2P_{3/2}$ states is considered. The large splitting ($\sim$1.8 GHz) in the $5s$ ground state means that atoms excited on the $F = 0 \rightarrow F' = 1$ and $F = 1 \rightarrow F' = 1$ hyperfine transitions are optically pumped to the $F = 1$ ($F = 0$) levels after an average of two (three) photon scattering events, respectively. The process of optical pumping tends to reduce the amplitudes and increase the width of these lines as compared to the closed $F = 1 \rightarrow F' = 2$ transition, and necessitates minimizing the number of photon scattering events per atom to obtain the best spectra. Second, the hyperfine splitting in the $5p\ ^2P_{3/2}$ state is roughly three times the natural linewidth of the transition, which modifies the fluorescence line shape by the interference between photon scattering pathways [50]. To minimize this effect, we use laser light linearly polarized at an angle $\theta_{\mathrm{m}} = \cos^{-1}(1/\sqrt{3})$ to the detector direction. This is the so-called magic angle at which the anisotropic part of the fluorescence emission is zero, interference between scattering paths disappears, and a symmetric line shape is recovered [50]. The relatively large solid angle of our collection optics of nearly $\pi/4$ steradians further suppresses the interference effect by roughly a factor 2.

Figure 2(b) shows three spectra obtained with our spectrometer. The upper two spectra are taken with a single-frequency probe laser, at two different probe laser intensities I_0. We label the spectra by the two-level saturation parameter $s = I_0/I_{\mathrm{sat}}$, where $I_{\mathrm{sat}} = \frac{\pi hc\Gamma}{3\lambda^3} = 82.5\ \mathrm{mW/cm}^2$ is the two-level saturation intensity for the transition. Solid red lines

TABLE III. Determining the dependence of energies and isotope shift factors on the assumed root-mean-squared nuclear charge radius R, in fm. Calculated values of electron attachments and isotope shift factors in different states with different values for the nuclear charge radius. The Dirac-Coulomb Hamiltonian at the analytical-response, relativistic coupled-cluster up to double excitations [(AR-)RCCSD] approximation is used. The $R = 4.55$ column corresponds to the AR-CCSD column in Table II.

	$R = 4.34$	$R = 4.54$	$R = 4.55$	$R = 4.56$	$R = 4.84$
EA values in cm^{-1}					
$5s\ ^2S_{1/2}$	60407.91	60407.69	60407.67	60407.66	60407.33
$5p\ ^2P_{1/2}$	31007.44	31007.43	31007.43	31007.43	31007.42
$5p\ ^2P_{3/2}$	30088.87	30088.86	30088.86	30088.86	30088.85
$6s\ ^2S_{1/2}$	18454.78	18454.75	18454.75	18454.74	18454.70
$6p\ ^2P_{1/2}$	12680.42	12680.41	12680.41	12680.41	12680.41
$6p\ ^2P_{3/2}$	12467.25	12467.25	12467.25	12467.25	12467.25
F MHz/fm^2					
$5s\ ^2S_{1/2}$	−3866.85	−3853.40	−3852.20	−3850.63	−3830.17
$5p\ ^2P_{1/2}$	−163.99	−163.38	−163.39	−163.26	−162.40
$5p\ ^2P_{3/2}$	−126.66	−126.22	−126.25	−126.14	−125.47
$6s\ ^2S_{1/2}$	−518.63	−516.82	−516.66	−516.45	−513.71
$6p\ ^2P_{1/2}$	−32.03	−31.92	−31.92	−31.89	−31.73
$6p\ ^2P_{3/2}$	−25.33	−25.24	−25.24	−25.22	−25.09
K^{NMS} GHz u					
$5s\ ^2S_{1/2}$	807.82	807.79	807.88	807.77	807.73
$5p\ ^2P_{1/2}$	366.64	366.63	366.68	366.63	366.67
$5p\ ^2P_{3/2}$	350.68	350.67	350.71	350.67	350.71
$6s\ ^2S_{1/2}$	273.87	273.86	273.87	273.86	273.85
$6p\ ^2P_{1/2}$	180.86	180.86	180.87	180.86	180.87
$6p\ ^2P_{3/2}$	175.74	175.74	175.75	175.74	175.75
K^{SMS} GHz u					
$5s\ ^2S_{1/2}$	1346.77	1346.49	1346.33	1346.49	1346.41
$5p\ ^2P_{1/2}$	342.32	341.77	341.68	341.72	341.79
$5p\ ^2P_{3/2}$	370.81	370.27	370.16	370.23	370.22
$6s\ ^2S_{1/2}$	175.67	175.61	175.59	175.60	175.60
$6p\ ^2P_{1/2}$	65.30	65.19	65.17	65.18	65.18
$6p\ ^2P_{3/2}$	75.45	75.34	75.32	75.33	75.33

show fits using a set of Lorentzian functions, where the full width at half maximum $\Gamma/(2\pi)$ is allowed to vary between resonances in order to account for optical pumping. For the spectrum at lower intensity, the relative line intensities agree well with the relative line intensities given in Fig. 2(a), indicating that optical pumping has been largely avoided. For the higher-intensity spectrum, we use the relative peak heights to estimate that when the laser is tuned to the $(F, F') = (1, 2)$ resonance, the atoms scatter, on average, six photons. This means that the effect of photon recoil shifts and broadens the resonance lines by, at most, 0.1 MHz. We note that the number of photon scattering events derived from the line intensities is a factor of two less than that derived using a simple two-level rate equation model and the estimated intensity of the probe light. The Lorentzian linewidth of the (1,2) resonances, unaffected by optical pumping, is $\Gamma/(2\pi) = 25.4(1.0)$ MHz. Fitting with a Voigt line shape resulted in a slightly reduced Lorentzian linewidth, $\Gamma/(2\pi) = 24.4(6)$ MHz, with a Gaussian linewidth of below 4 MHz (full width at half maximum), corresponding to a transverse velocity spread of below 3.1 m/s. The radiative lifetime extracted from the Voigt fits, $\tau = 1/\Gamma$, is a few percent below that reported by Carlsson *et al.* [51], which we attribute to the effect of a residual magnetic field in our detector, measured to be ∼0.3 G.

The absolute frequencies of the line centers from six spectra, taken over two days and using a range of probe laser intensities, varied by less than 2 MHz (standard deviation), and intervals between resonance lines varied by less than 1.5 MHz (standard deviation). The absolute frequency uncertainty is dominated by the 10 MHz uncertainty of the wave meter at 656 nm; in a previous experiment using the same spectrometer, we found agreement with the precisely measured $^1S_0 \rightarrow\ ^1P_1$ 399 nm line in Yb at the 10 MHz level [47]. Doppler shifts due to misalignment of the probe laser and atomic beams is, at most, 2 MHz, which we estimate by plotting the fitted line centers versus forward velocity in the atomic beam, and extrapolating to zero velocity. We extract the magnetic dipole hyperfine interaction constants A_{107} and A_{109} in each state for the two Ag isotopes and present these in Table IV. The ground-state splittings agree, with high accuracy, with the microwave measurements [52,53] to within 2.5 MHz (^{109}Ag) and 0.4 MHz (^{107}Ag), and for the excited state, we agree with the quantum beat spectroscopy measurements of Carlsson *et al.* [51] to better than 0.4 MHz. This suggests that the isotope shift between ^{107,109}Ag measured from the same spectra may have an uncertainty of 2–3 MHz due to the uncertainty of the wave-meter frequency measurements.
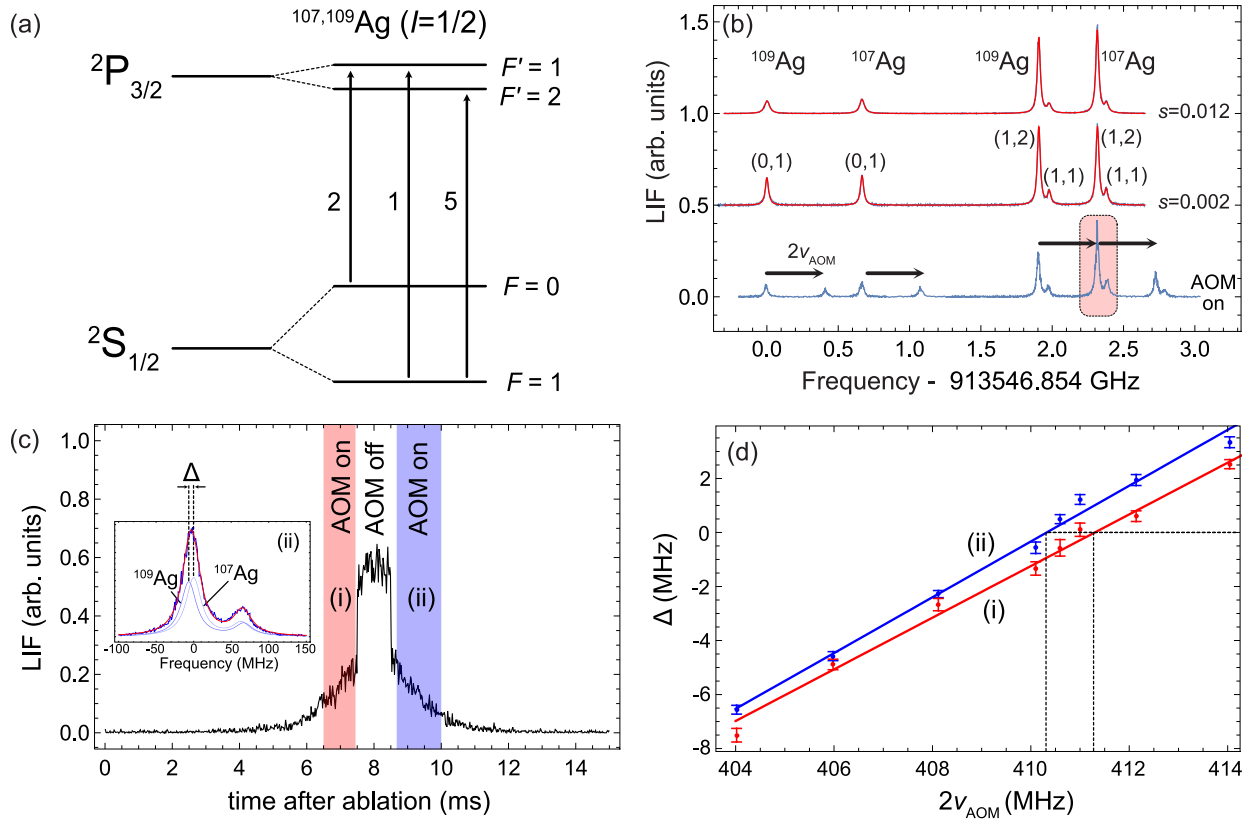
FIG. 2. Laser-induced fluorescence spectroscopy of a buffer gas cooled Ag atomic beam. (a) Level scheme for the $^2S_{1/2} \rightarrow {}^2P_{3/2}$ transition in ^{107,109}Ag. The relative intensities of the transitions are indicated. (b) Example spectra taken using a single-frequency probe beam with $s = 0.012$ (upper), a single-frequency probe beam with $s = 0.002$ (middle), and a two-frequency probe beam whose frequencies are separated by $2\nu_{AOM} \approx 410$ MHz (lower). Resonance lines are labeled by isotope and total angular momentum numbers (F, F') for the transition. The red shaded box indicates the region where the (1,2) transitions of ^{107,109}Ag are almost overlapping. (c) Example time-of-flight trace of the fluorescence when using the double-pass acousto-optic modulator (AOM) as discussed in the text, illustrating the observation windows used in the analysis. A sudden change in the fluorescence signal occurs when the AOM is switched on or off. The inset shows a spectrum using observation window (ii), and the fitted frequency offset Δ between the (1,2) lines of the Ag isotopes. The contributions of the individual isotopes are shown in transparent blue, with the solid red line their sum which is the combined fit function. (d) A plot of the fitted value of Δ vs $2\nu_{AOM}$ for observation windows (i) and (ii), used to extract the isotope shift of the (1,2) lines.

To improve the accuracy of our isotope shift measurements, we introduced a single acousto-optical modulator (AOM) into the optical setup, operated in double-pass configuration using a cat-eye lens. The AOM is driven at a radio frequency ν_{AOM}, which can be varied via a voltage controlled oscillator, and is monitored using a radio frequency counter. We deliberately allow both the zeroth-order (i.e., unshifted) and twice-shifted beams to be present, such that the probe laser light is now composed of two frequency components separated by $2\nu_{AOM}$, and whose spatial overlap and pointing varies by less than 0.4 mrad as ν_{AOM} is varied. An example spectrum is shown in the lower trace of Fig. 2(b), where arrows show the displacement in the frequency axis introduced by the AOM. We choose ν_{AOM} to be around 200 MHz such that the frequency-shifted component of the probe beam excites the ^{107}Ag, $F = 1 - F' = 2$ transition, while the other component simultaneously excites this transition in ^{109}Ag. This enables detection of both isotopes while only scanning a small ($\sim$200 MHz) range with the laser, indicated by the red shaded box in the spectrum. Moreover, we can rapidly switch

between single- and dual-frequency probe light as atoms fly through the detector via the rf driving power to the AOM.

Figure 2(c) shows a time-of-flight fluorescence trace using the AOM method, and with the laser tuned to the (1,2) ^{107}Ag resonance. The rf power to the AOM is set to give equal optical power in the two frequency components, and is switched off for roughly 200 μs as the atoms fly through the detector. We use the fluorescence within this observation window for a "reference spectrum" in order to fix the ^{107}Ag isotope position in each measurement. This largely removes contributions to the IS from any slow drift in the wave-meter frequency axis over timescales longer than a minute. The shaded regions in Fig. 2 labeled (i) and (ii) are observation windows for which both frequency components are present in the probe light. We fit spectra derived from these observation windows to a model containing the resonances of both isotopes, where the hyperfine splittings are fixed to those given in Table IV, the ^{107}Ag (1,2) resonance is fixed to that measured in the reference spectrum, and the natural abundance ratio determines the total contribution from each isotope to the spectrum.

TABLE IV. Summary of the experimental results for the $5s\,^2S_{1/2} \rightarrow 5p\,^2P_{3/2}$ transition in ^{107,109}Ag, and comparison with the literature values. All values are given in MHz. Absolute frequencies of hyperfine lines for isotope α are labeled as $\nu_\alpha(F, F')$ and $\bar{\nu}_\alpha$ denotes the gravity center for this isotope. $\bar{\nu}_{nat.}$ is the mean of the gravity centers for the two isotopes, weighted by the natural isotopic abundance, which approximates the observed line center in a low-resolution measurement with a naturally abundant sample. $\delta\nu_{109,107}(1, 2) = \nu_{107}(1, 2) - \nu_{109}(1, 2)$. $\delta\bar{\nu}_{109,107} = \bar{\nu}_{107} - \bar{\nu}_{109}$.

	This work	Literature
$\nu_{109}(1, 2)$	913 548 760(20)	
$\nu_{107}(1, 2)$	913 549 171(20)	
$A_{109}(^2P_{3/2})$	$-36.9(3)$	$-36.7(7)$ [51]
$A_{109}(^2S_{1/2})$	$-1979.4(1.1)$	$-1976.932\,075(17)$ [53]
$A_{107}(^2P_{3/2})$	$-31.7(6)$	$-31.7(7)$ [51]
$A_{107}(^2S_{1/2})$	$-1713.0(8)$	$-1712.512\,111(18)$ [53]
$\bar{\nu}_{109}$	913 548 293(20)	
$\bar{\nu}_{107}$	913 548 766(20)	
$\bar{\nu}_{nat.}$	913 548 539(20)	913 548 593(60) [33]
$\delta\nu_{109,107}(1, 2)$	410.9(6)	
$\delta\bar{\nu}_{109,107}$	473.2(7)	467(4) [24]
		476(10) [54]

This leaves only the offset frequency Δ between the (1,2) resonances of ^{107,109}Ag as a free parameter, beside a common amplitude term and a y-axis offset. The inset to Fig. 2 displays an example spectrum with $2\nu_{AOM} = 404.02$ MHz, showing the two isotope components of the signal and the interval Δ in the underlying fit function.

We repeat this procedure for different values of $2\nu_{AOM}$ and plot Δ versus $2\nu_{AOM}$ in Fig. 2(d). In the ideal case, this should result in a linear relationship with a gradient 1, whose x-axis intercept (i.e., where $\Delta = 0$) returns the isotope shift between the (1,2) lines of the two Ag isotopes. The linear fits to the data in observation windows (i) and (ii) have slightly different intercepts, which we attribute to a small residual misalignment of the probe light to the atoms, and the atoms in the two observation windows having slightly different forward velocities. The slopes of the two curves are 0.96(2) and 1.03(2) in regions (i) and (ii), respectively. We take the average of the two intercepts as the x-axis intercept, and half their difference as the 67% confidence interval, and apply small corrections to this value to arrive at our value for the true isotope shift as follows. First, we consider the residual alignment difference between the two frequency components in the probe light, which, for a forward velocity of 120 m/s, tends to reduce the line separation by 150 kHz. Second, the spectral intensity of the probe light near the ^{107}Ag resonance is about a factor of 4 larger (i.e., $s \approx 0.016$) in the reference spectrum, which would shift the (1,2) line center of ^{107}Ag in the reference spectrum by $+70$ kHz. We both correct for these effects and increase the systematic error bar accordingly. Third, the background magnetic field in the detector ($\sim$0.3 G) leads to Zeeman shift-induced broadening of the hyperfine lines and potentially to a small differential shift. Since the nuclear spins of ^{107,109}Ag are identical, and the nuclear magnetic moments are within about 15% of one another [55], this effect is negligible. AC Stark shifts of the $^2P_{3/2}$ and $^2S_{1/2}$ states by the excitation light

are well below the kHz level for the intensities used in our measurements and can be neglected. The result, $\delta\nu_{109,107} = \nu_{107}(1, 2) - \nu_{109}(1, 2) = 410.9(6)$ MHz, is consistent with that measured using the wide range, single-frequency probe data, 410.7(7) MHz, though the latter has a few MHz of systematic uncertainty associated with the linearity of the wave meter. Our procedure is robust to relaxing many assumptions about the underlying line-shape model. For example, fitting the overlapping (1,1) resonances as a single Lorentzian line changes $\delta\nu_{109,107}(1, 2)$ by less than 0.1 MHz. Varying the contribution of ^{107,109}Ag to the overlapping (1,2) lines also results in a value for $\delta\nu_{109,107}(1, 2)$, consistent within 0.1 MHz. Such a signal imbalance only significantly changes the slope observed in Fig. 2(d).

In deriving an improved value for the isotope shift of the $5s\,^2S_{1/2} \rightarrow 5p\,^2P_{3/2}$ gravity center, we take advantage of the $^2S_{1/2}$ hyperfine-structure measurements of [53], whose stated uncertainty is below 0.1 kHz. We use the values in Table IV for the hyperfine splitting of the $^2P_{3/2}$ states, and use the result of Fig. 2(d) to fix the isotope shift of the (1,2) lines. This interval contributes most to the uncertainty of the gravity center isotope shift, and therefore dominates the error bar.

V. MEAN-SQUARED RADIUS DIFFERENCE

A. Between stable isotope pairs

We now combine our calculations of F and K with optical isotope shifts to estimate the mean-squared charge radius difference of the stable isotope pair, $\delta r^2_{109,107}$. The calculated relative transition field shift factors, $F(i) - F(5s\,^2S_{1/2})$, span a range of $-3223(26)$ to $-3683(43)$ GHz/fm^2, which is an order of magnitude larger than their individual uncertainties (see Table II). Thus, a useful consistency check of our F and K calculations, as well as the experimental ISs, is satisfied when applying Eq. (1) to each optical transition returns similar values of $\delta r^2_{109,107}$. The relative ISs are calculated with a Ritz-type analysis (see, e.g., [12]) of our measurement and those given in [56–60]. The results are given in Table V.

The standard deviation of the radii extracted from individual transitions is 0.003 fm^2. It is slightly larger than the 0.002 fm^2 which we would expect from the uncorrelated uncertainties. This could indicate possible underestimated uncertainties in the experiment and/or our calculation. To account for it, we conservatively add the standard deviation as another source of systematic uncertainty to all of our recommended values of δr^2.

Our final recommended value for $\delta r^2_{109,107}$ including the above uncertainties is within 1.0 combined standard uncertainties from $\delta r^2_{109,107} = (R_k^{109}/V_2^{109})^2 - (R_k^{107}/V_2^{107})^2$, where the Barrett-equivalent moments R_k are measured with muonic atom x-ray spectroscopy [2], and the proportionality factors between the Barrett and second charge moment $V_2 \equiv R_k/R$ are estimated with a Fermi distribution, to which we added a relative shape-variation uncertainty. It is illuminating to note that in both muonic and electronic silver, it is the (unknown) shape change which dominates the error in the extracted radii. This motivates one to perform an elastic electron scattering experiment to determine the shape change. The marginal agreement between radii differences extracted all-optically and from

TABLE V. Extraction of the mean-squared radius difference, $\delta r^2_{109,107} \equiv r^2_{107} - r^2_{109}$ in fm^2, of the stable isotopes of Ag via different optical transitions from the ground state. $\delta \nu_{109,107} \equiv \nu_{107} - \nu_{109}$ are the center-of-gravity isotope shifts in MHz, estimated from the indicated data sources, including this work (TW). The corresponding $\delta r^2_{109,107}$ in fm^2 are extracted employing the factors given in Table II. The uncertainties are denoted with subscripts according to experiment (expt), uncertainties in our calculated isotope shift factors (K, F), standard deviation from unweighted mean (std), systematic uncertainty from nuclear shape variation (NS), and uncertainty in extraction from muonic atoms due to nuclear polarization (NP).

Interval	Source	$\delta \nu_{109,107}$	$\delta r^2_{109,107}$
$5s\ ^2S_{1/2} - 5p\ ^2P_{1/2}$	[56,57]	473(4)	$-0.207(1)_{\text{expt}}(3)_{K,F}$
$5s\ ^2S_{1/2} - 5p\ ^2P_{3/2}$	TW	473.2(7)	$-0.204(0)_{\text{expt}}(3)_{K,F}$
$5s\ ^2S_{1/2} - 6s\ ^2S_{1/2}$	TW, [56–58]	368(7)	$-0.212(2)_{\text{expt}}(3)_{K,F}$
$5s\ ^2S_{1/2} - 6p\ ^2P_{3/2}$	[59,60]	414.0(6)	$-0.207(0)_{\text{expt}}(3)_{K,F}$
Final			$-0.207(3)_{\text{std}}(3)_{K,F}(4)_{\text{NS}}$
Muonic Ag	[2]		$-0.198(0)_{\text{expt}}(4)_{\text{NP}}(5)_{\text{NS}}$
Interpolated	[25]		$-0.148(31)$
Compilation	[61]		$-0.148(1)$

muonic atoms is expected considering recent work in the medium-mass region [7,18,20], pointing to the need to reanalyze the cascade energies with modern tools (e.g., [62–69]). It is also worth noting that in Ref. [24], a more conservative uncertainty estimate for the muonic data was employed.

We conclude this section by focusing on the IS of the fine structure of the $5p$ doublet. Calculating it from the factors of Table II and the recommended $\delta r^2_{109,107}$ from Table VI results in $-8.3(4)$ MHz, in tension with the experimental value of 0 ± 4 MHz, whose uncertainty is completely decided by a single photoelectric measurement [56]. Extending precision laser spectroscopy to the IS of the $5s\ ^2S_{1/2} - 5p\ ^2P_{1/2}$ 338 nm line could help to shed light on this issue. The experimental method detailed in this article could be straightforwardly applied.

B. Among isotope and isomer chains

We interpret the ISs measured in radioisotopes of Ag in terms of δr^2. The nuclei are divided into three groups. The first consists of those whose ISs were measured only for the $5s\ ^2S_{1/2} - 5p\ ^2P_{3/2}$ 328 nm line (Refs. [24,26,27]).

TABLE VI. Extraction of the difference in mean-squared nuclear charge radius, δr^2 in fm^2, between radioactive silver isotopes and isomers, from optical isotope shifts $\delta \nu$ in GHz. When two references are given, the value is their weighted average. Numbers in italics are an input to the King Plot of Fig. 3. $\nu^{328,\text{KP}}_{109,A}$ is the mean and standard deviation of the posterior distribution of the 328 nm line isotope shift which is output by the fit. The δr^2 are calculated from $\nu^{328}_{109,A}$ and, when available, $\nu^{328,\text{KP}}_{109,A}$, using the isotope shift factors from Table II, taking into account the corrections given in Table III. The uncertainties in parentheses are tied to the experimental isotope shift measurements, and those in square brackets are the total systematic uncertainties discussed in Sec. V A. The absolute radius can be obtained by adding $R(^{109}\text{Ag}) = 4.564(2)$ fm [2] in quadrature. The last column includes the ladder-type difference for ground-state nuclei and the isomer shifts for isomers.

A	$\delta \nu^{548}_{109,A}$	Ref.	$\delta \nu^{328}_{109,A}$	Ref.	$\delta \nu^{328,\text{KP}}_{109,A}$	$\delta r^2_{109,A}$	Ref. [24]	Ref. [25]	$\delta r^2_{A,A+2}$
96			$2.64^{+1.1}_{-0.8}$	[24]		$-1.26^{+22}_{-31}[4]$	$-1.21^{+27}_{-19}[14]^\dagger$		$-0.20(27)[1]$
97			4.36(28)	[24,26]		$-1.69(8)[5]$	$-1.55(8)[15]$		0.41(8)[1]
98			3.66(21)	[24,26]		$-1.45(6)[4]$	$-1.36(6)[13]$		0.31(8)[1]
99			3.20(9)	[24,26]		$-1.28^{+2}_{-3}[4]$	$-1.20^{+3}_{-2}[12]^\dagger$		0.27(5)[1]
100			2.85(20)	[24,26]		$-1.14(6)[3]$	$-1.02(8)[11]$		0.43(7)[1]
101	*4.672(5)*	[25]	*2.54(23)*	[24,26]	2.55(17)	$-1.02(5)[3]$	$-0.98(10)[10]$	$-0.670(3)[135]$	0.31(5)[1]
102			1.60(17)	[24]		$-0.712(48)[20]$	$-0.67^{+5}_{-4}[8]^\dagger$		0.06(6)[0]
103	*3.302(4)*	[25]	*1.58(30)*	[24]	1.74(8)	$-0.711(23)[24]$	$-0.63(7)[7]$	$-0.482(2)[98]$	0.313(24)[10]
104	*2.939(3)*	[25]	*1.71(22)*	[24]	1.65(14)	$-0.648(39)[22]$	$-0.61(6)[6]$	$-0.416(2)[83]$	
105	1.926(6)	[25]			0.894(22)	$-0.397(6)[13]$		$-0.296(2)[63]$	0.193(6)[6]
107	*0.9781(5)*	[59]	*0.4732(7)*	TW		$-0.207(0)[6]$	$-0.198(2)[20]$	$-0.148(1)[31]$	0.207(0)[6]
114			$-0.850(3)$	[24]		0.408(1)[14]	0.384(1)[50]		0.116(3)[4]
115			$-0.995(5)$	[24]		0.480(1)[16]	0.454(3)[60]		0.114(2)[4]
116			$-1.040(9)$	[24]		0.524(3)[18]	0.500(10)[60]		0.107(3)[4]
117			$-1.181(6)$	[24]		0.595(2)[20]	0.568(3)[70]		0.107(2)[4]
118			$-1.203(5)$	[24]		0.631(1)[21]	0.607(3)[80]		0.108(2)[3]
119			$-1.348(5)$	[24]		0.702(1)[23]	0.675(3)[90]		0.090(2)[4]
120			$-1.379(4)$	[24]		0.740(1)[25]	0.715(2)[90]		
121			$-1.461(3)$	[24]		0.791(1)[26]	0.767(1)[100]		
									$\delta r^2_{A,Am}$
99m			3.58(68)	[24,26]		$-1.39(19)[5]$	$-1.18^{+26}_{-22}[12]$		$-0.11(19)[0]$
101m			2.40(24)	[26]		$-0.98(7)[3]$	$-0.91(6)[10]$		0.04(8)[0]
105m	2.229(10)	[25]			1.21(8)	$-0.485(21)[16]$		$-0.321(2)[65]$	$-0.088(22)[3]$
106m	2.049(30)	[25]			1.30(18)	$-0.474(52)[16]$		$-0.271(4)[52]$	
108m			0.443(9)	[27]		$-0.159(3)[5]$		$-0.120(13)[20]$	
110m			$-0.689(60)$	[27]		0.0551(17)[18]		0.036(5)[16]	

†Our analysis suggests that when adopting the tabulated asymmetric statistical uncertainties in $\delta \nu^{328}_{109,A}$, the signs of the corresponding uncertainties in $\delta r^2_{109,A}$ should be swapped as compared with those given in Table 1 and Fig. 2 of Ref. [24].
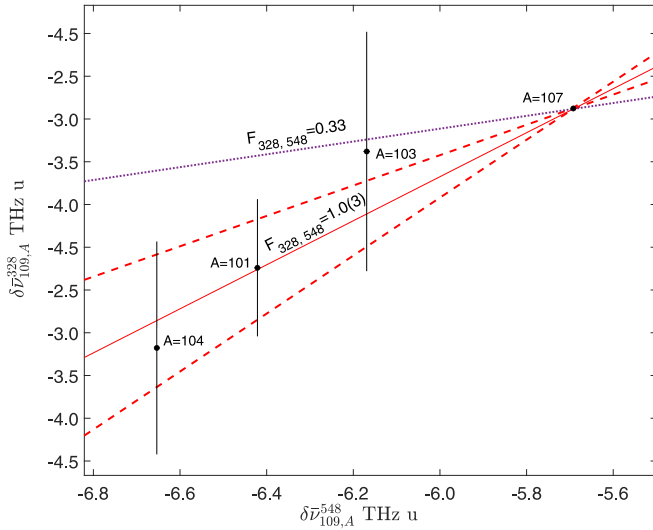
FIG. 3. Two-dimensional King Plot whose data points are given in italics in Table VI. The vertical axis is the reduced IS in the $5s\ ^2S_{1/2}-5p\ ^2P_{3/2}$ transition. The horizontal axis is the reduced isotope shift in the $4d^9 5s^2\ ^2D_{5/2}-6p\ ^2P_{3/2}$ transition. The resulting slope (full line) lies two standard deviations (dashed lines) away from that calculated empirically (dotted line) in [25].

Here, $\delta r^2_{109,A}$ can be directly estimated using our calculated IS factors, including the systematic uncertainties discussed in the previous section. The results are given in Table VI. The second group includes the four nuclei whose ISs were measured for both 328 nm and $4d^9 5s^2\ ^2D_{5/2}-6p\ ^2P_{3/2}$ 548 nm lines (data from this work and Refs. [24–26,59], italicized in Table VI). Because the 548 nm line involves a $4d^9 5s^2$ configuration, i.e., a $4d$-hole state, accurately calculating $F_{548} \equiv F(6p\ ^2P_{3/2}) - F(4d^9 5s^2\ ^2D_{5/2})$ and $K_{548} \equiv K(6p\ ^2P_{3/2}) - K(4d^9 5s^2\ ^2D_{5/2})$ is beyond the scope of this article. We interpret these data by making use of a two-dimensional KP linear equation,

$$\delta\bar{\nu}^{328}_{A,A'} \simeq K_{328,548} + F_{328,548}\,\delta\bar{\nu}^{548}_{A,A'}, \qquad (24)$$

where $\delta\bar{\nu}^i_{A,A'} \equiv \delta\nu^i_{A,A'}/\mu_{A,A'}$, $F_{328,548} \equiv F_{328}/F_{548}$, and $K_{328,548} \equiv K_{328} - F_{328,548}K_{548}$. The higher-order corrections to Eq. (1) affect the validity of Eq. (24). The largest effect stems from the variation in nuclear shape, which is of the order of 2% of the field shifts of the two transitions. Thus the maximal change in the slope $F_{328,548}$ is 4%, which is negligible compared with the statistical uncertainty in it, which is 30%. A Monte Carlo linear regression, shown in Fig. 3, returns a slope $F_{328,548} = 1.0(3)$ and intercept $K_{328,548} = 3.4(1.9)$ THz u. It also results in posterior ISs for the cooling line, which we denote $\delta\nu^{328,\mathrm{KP}}_{109,A}$, given in Table VI, along with their corresponding radii. The third group consists of nuclei for which measurements exist only for the 548 nm line. We use the joint distribution of the slope and intercept to project their ISs from the 548 nm line to the 328 nm line. The results are also given in Table VI, with the corresponding radii.

The fit results can be used to check for the reasons for inconsistencies found in the literature. The fitted slope deviates by two of its standard deviations from $F^{\mathrm{SE}}_{548,328}$

$F^{\mathrm{SE}}_{328,548} = 0.33(3)$, estimated from the semi-empirical FS factors given in [25]. Combining our calculated factors for the cooling line with the fitted slope and intercept, we find $F_{548} = -3^{+1}_{-2}$ GHz/fm^2 and $K_{548} = -2^{+2}_{-1}$ THz u. Although it is roughly estimated, our FS factor is four combined standard errors away from the semi-empirical estimation $F^{\mathrm{SE}}_{548} = -12(1)$ GHz/fm^2 [25]. Indeed, the authors of Ref. [25] observed that when F^{SE}_{548} was combined with $\delta r^2_{109,107}$ from muonic atoms, a surprising crossing of isotopic chains appeared around $Z = 50$. To remedy this issue, they elected to interpolate $\delta r^2_{109,107}$ from that of neighboring isotones. These epicycles resulted in $K^{\mathrm{SE}}_{548} = 4.4(2.7)$ THz u, which was considered to agree with the Hartree-Fock calculation by Bauche [70]. However, as seen in Table II, a Hartree-Fock calculation cannot reproduce the sign of the SMS, which value dominates that of the total MS. Considerably reducing the errors of the data points in Fig. 3, or introducing new ones via measurements, would help shed light on these issues while reducing uncertainties in the extracted radii.

Our recommended $\delta r^2_{109,A}$ are compared with prior extractions in Table VI and Fig. 1. Although significantly different IS factors are used, we find agreement with the radii given in Ref. [24] within uncertainties. This is due to the mitigating effect of enforcing $\delta r^2_{109,107}$ from muonic atoms. However, the all-optical radii have smaller uncertainties, by up to a factor of 5 (for $\delta r^2_{109,105}$). This motivates more accurate IS measurements for the neutron-deficient Ag, whose radii uncertainties are now dominated by experiment. A larger disagreement is observed when comparing our results with those of the GSI group [25], with the largest deviation (4σ) for $\delta r^2_{109,106m}$. This is due to the reasons described above; namely, the different estimation of $\delta r^2_{109,107}$ (see Table V) and the highly different F_{548}. Whereas most of the nuclei whose ISs were measured with the 548 nm line at GSI were also later measured with the cooling line, ^{105}Ag, ^{105m}Ag, and ^{106m}Ag were only measured with the 548 nm line. This work endows them with reliable and precise $\delta r^2_{109,A}$.

We conclude this section by comparing $\delta r^2_{109,A}$ from this work and the value calculated by state-of-the-art density functional theory (DFT) as done in [24] and shown in Fig. 1. Focusing first on the neutron rich isotopes, we see agreement for the odd-odd nuclei and a disagreement for the odd-even ones. On the proton-rich side, an agreement is seen for all nuclei except for ^{96}Ag, as discussed in [24], and ^{102}Ag, which lies 6 standard errors from the DFT calculation. These discontinuities are further emphasized when looking at the ladder-type differences, given in the last column of Table VI.

VI. SUMMARY AND OUTLOOK

Nuclear charge radius differences in the silver isotopic chain deviate between experiments at the few σ level, as seen in Fig. 1. To find the origin of these deviations and reconcile them, we performed high-accuracy calculations of isotope shift factors in the low-lying states of atomic silver (Tables I and II), as well as precise spectroscopic measurements in the silver $5s\ ^2S_{1/2}-5p\ ^2P_{3/2}$ line (Table IV), and combined this information in a global analysis (Tables V and VI).

We find that discrepancies in the reported values of δr^2 are largely the result of the field shift factors F used to extract them from the experimental data, rather than discrepancies between experiments. Our measurement of the center-of-gravity isotope shift is within 2 combined standard errors from a recent collinear laser spectroscopy measurement [24]. This difference is too small to explain the tensions with earlier studies, narrowing down the suspects to the used IS factors and/or the mean-squared radius difference of the stable pair. To test the latter, we extracted the mean-squared radius difference of the stable pair from the isotope shifts of four transitions to the ground state, two of which make use of our measurement in the 328 nm line (see Table V). We find a reasonable agreement between these radii, which allows one to estimate the accuracy of the calculated IS factors. Based on this, we recommended a radius difference for the stable pair. It is one combined standard error away from the one extracted from muonic atom cascade x-ray spectroscopy [2], and two standard errors away from the value used in prior works [25,26], which was interpolated from neighboring nuclei. The three values of the mean-squared radius differences used by us and in prior works partially explain the disagreements in the silver chain, which must thus originate from the choice of field shift factor. We show this by making a projection of our calculated factors from the $5s\ ^2S_{1/2} - 5p\ ^2P_{3/2}$ line to the $4d^9 5s^2\ ^2D_{5/2} - 6p\ ^2P_{3/2}$ line using a King Plot (Fig. 3), which also benefits from our precise IS measurement. The projected factors of the 548 nm line disagree by four combined standard errors with the ones evaluated semi-empirically, thus pointing out that this is the main culprit of the disagreements.

Having shed light on prior disagreements, we provide in Table VI transparent and reliable mean-squared radius differences in the silver isotopic chain. Their trend is found to be generally consistent with that from a state-of-the-art nuclear theory calculation. Nevertheless, the calculated shape-staggering effect is overestimated on the neutron-rich side, and there are discontinuities around $A = 96$ and $A = 102$ which call for further attention, as seen in Fig. 1. With the much smaller systematic uncertainties afforded by this work, the radii of proton-rich silver nuclei could now be greatly improved with more accurate measurements, and the maximum information can be extracted from new measurements extending even further towards the drip lines [71].

[1] X. F. Yang, S. J. Wang, S. G. Wilkins, and R. F. Garcia Ruiz, Laser spectroscopy for the study of exotic nuclei, Prog. Part. Nucl. Phys. **129**, 104005 (2023).

[2] G. Fricke and K. Heilig, *Nuclear Charge Radii*, edited by H. Schopper (Springer-Verlag, Berlin, 2004), Vol. 454.

[3] K. W. Ford and J. G. Wills, Muonic atoms and the radial shape of the nuclear charge distribution, Phys. Rev. **185**, 1429 (1969).

[4] W. H. King, Comments on the article "Peculiarities of the isotope shift in the samarium spectrum," J. Opt. Soc. Am. **53**, 638 (1963).

[5] A. Adamczak, A. Antognini, N. Berger, T. E. Cocolios, N. Deokar, Ch. E. Düllmann, A. Eggenberger, R. Eichler, M. Heines, H. Hess *et al.*, Muonic atom spectroscopy with microgram target material, Eur. Phys. J. A **59**, 15 (2023).

[6] M. Heines, L. Antwis, S. Bara, B. Caerts, T. E. Cocolios, S. Eisenwinder, J. Fletcher, T. Kieck, A. Knecht *et al.*, Muonic x-ray spectroscopy on implanted targets, Nucl. Instrum. Methods Phys. Res. Sect. B **541**, 173 (2023).

[7] M. L. Bissell, T. Carette, K. T. Flanagan, P. Vingerhoets, J. Billowes, K. Blaum, B. Cheal, S. Fritzsche, M. Godefroid *et al.*, Cu charge radii reveal a weak sub-shell effect at $N = 40$, Phys. Rev. C **93**, 064318 (2016).

[8] T. J. Procter, J. Billowes, M. L. Bissell, K. Blaum, F. C. Charlwood, B. Cheal, K. T. Flanagan, D. H. Forest, S. Fritzsche, Ch. Geppert *et al.*, Nuclear mean-square charge radii of $^{63,64,66,68-82}$Ga nuclei: No anomalous behavior at $N = 32$, Phys. Rev. C **86**, 034329 (2012).

[9] T. J. Procter, J. A. Behr, J. Billowes, F. Buchinger, B. Cheal, J. E. Crawford, J. Dilling, A. B. Garnsworthy, A. Leary, C. D. P. Levy *et al.*, Direct observation of an isomeric state in ^{98}Rb and nuclear properties of exotic rubidium isotopes measured by laser spectroscopy, Eur. Phys. J. A **51**, 23 (2015).

[10] Y. P. Gangrsky, K. P. Marinova, S. G. Zemlyanoi, I. D. Moore, J. Billowes, P. Campbell, K. T. Flanagan, D. H. Forest, J. A. R. Griffith *et al.*, Nuclear charge radii of neutron deficient titanium isotopes ^{44}Ti and ^{45}Ti, J. Phys. G: Nucl. Part. Phys. **30**, 1089 (2004).

[11] K. Blaum, W. Geithner, J. Lassen, P. Lievens, K. Marinova, and R. Neugart, Nuclear moments and charge radii of argon isotopes between the neutron-shell closures $N = 20$ and $N = 28$, Nucl. Phys. A **799**, 30 (2008).

[12] B. Ohayon, H. Rahangdale, A. J. Geddes, J. C. Berengut, and G. Ron, Isotope shifts in ^{20,22}Ne: Precision measurements and global analysis in the framework of intermediate coupling, Phys. Rev. A **99**, 042503 (2019).

[13] B. Ohayon, R. F. G. Ruiz, Z. H. Sun, G. Hagen, T. Papenbrock, and B. K. Sahoo, Nuclear charge radii of Na isotopes: Interplay of atomic and nuclear theory, Phys. Rev. C **105**, L031305 (2022).

[14] K. König, J. C. Berengut, A. Borschevsky, A. Brinson, B. A. Brown, A. Dockery, S. Elhatisari, E. Eliav, R. F. G. Ruiz *et al.*, Nuclear charge radii of silicon isotopes, Phys. Rev. Lett. **132**, 162502 (2024).

[15] B. K. Sahoo, A. R. Vernon, R. F. G. Ruiz, C. L. Binnersley, J. Billowes, M. L. Bissell, T. E. Cocolios, G. J. Farooq-Smith, K. T. Flanagan *et al.*, Analytic response relativistic coupled-cluster theory: The first application to indium isotope shifts, New J. Phys. **22**, 012001 (2020).

[16] Á. Koszorús, X. F. Yang, W. G. Jiang, S. J. Novario, S. W. Bai, J. Billowes, C. L. Binnersley, M. L. Bissell, T. E. Cocolios, B. S. Cooper *et al.*, Charge radii of exotic potassium isotopes challenge nuclear theory and the magic character of $N = 32$, Nat. Phys. **17**, 439 (2021).

[17] J. S. Schelfhout and J. J. McFerran, Isotope shifts for $^1S_0 - {}^3P_{0,1}^o$ Yb lines from multiconfiguration Dirac-Hartree-Fock calculations, Phys. Rev. A **104**, 022806 (2021).

[18] B. Ohayon, S. Hofsäss, J. E. Padilla-Castillo, S. C. Wright, G. Meijer, S. Truppe, K. Gibble, and B. K. Sahoo, Isotope shifts in cadmium as a sensitive probe for physics beyond the standard model, New J. Phys. **24**, 123040 (2022).

[19] J. S. Schelfhout and J. J. McFerran, Multiconfiguration Dirac-Hartree-Fock calculations for Hg and Cd with estimates for unknown clock-transition frequencies, Phys. Rev. A **105**, 022805 (2022).

[20] B. K. Sahoo and B. Ohayon, All-optical differential radii in zinc, Phys. Rev. Res. **5**, 043142 (2023).

[21] J. Karthein, C. M. Ricketts, R. F. Ruiz, J. Billowes, C. L. Binnersley, T. E. Cocolios, J. Dobaczewski, G. J. Farooq-Smith, K. T. Flanagan, G. Georgiev *et al.*, Electromagnetic properties of indium isotopes elucidate the doubly magic character of ^{100}Sn, arXiv:2310.15093.

[22] G. Penyazkov, S. D. Prosnyak, A. E. Barzakh, and L. V. Skripnikov, Refined theoretical values of field and mass isotope shifts in thallium to extract charge radii of Tl isotopes, J. Chem. Phys. **158**, 114110 (2023).

[23] L. V. Skripnikov, S. D. Prosnyak, A. V. Malyshev, M. Athanasakis-Kaklamanakis, A. J. Brinson, K. Minamisono, F. C. P. Cruz, J. R. Reilly, B. J. Rickey, R. Ruiz *et al.*, Isotope shift factors with quantum electrodynamics effects for many-electron systems: A study of the nuclear charge radius of ^{26m}Al, arXiv:2404.13369.

[24] M. Reponen, R. P. de Groote, L. Al Ayoubi, O. Beliuskina, M. L. Bissell, P. Campbell, L. Cañete, B. Cheal, K. Chrysalidis, C. Delafosse *et al.*, Evidence of a sudden increase in the nuclear size of proton-rich silver-96, Nat. Commun. **12**, 4596 (2021).

[25] U. Dinger, J. Eberz, G. Huber, R. Menges, R. Kirchner, O. Klepper, T. Kühl, and D. Marx, Nuclear moments and change in the charge radii of neutron-deficient silver isotopes, Nucl. Phys. A **503**, 331 (1989).

[26] R. Ferrer, N. Bree, T. E. Cocolios, I. G. Darby, H. De Witte, W. Dexters, J. Diriken, J. Elseviers, S. Franchoo *et al.*, In-gas-cell laser ionization spectroscopy in the vicinity of ^{100}Sn: Magnetic moments and mean-square charge radii of $N = 50$–54 Ag, Phys. Lett. B **728**, 191 (2014).

[27] W. Fischer, H. Hühnermann, and T. Meier, Nuclear moments and optical isotope shifts of ^{108m}Ag and ^{110m}Ag, Z. Phys. A **274**, 79 (1975).

[28] S. A. Blundell, P. E. G. Baird, C. W. P. Palmer, D. N. Stacey, and G. K. Woodgate, A reformulation of the theory of field isotope shift in atoms, J. Phys. B **20**, 3663 (1987).

[29] C. S. Kischkel, M. Baumann, and E. Kummel, Two-photon spectroscopy of some even-parity levels in neutral ytterbium, J. Phys. B **24**, 4845 (1991).

[30] B. K. Sahoo, G. Gopakumar, R. K. Chaudhuri, B. P. Das, H. Merlitz, U. S. Mahapatra, and D. Mukherjee, Magnetic dipole hyperfine interactions in ^{137}Ba$^+$ and the accuracies of the neutral weak interaction matrix elements, Phys. Rev. A **68**, 040501(R) (2003).

[31] B. K. Sahoo, Appraising nuclear-octupole-moment contributions to the hyperfine structures in ^{211}Fr, Phys. Rev. A **92**, 052506 (2015).

[32] H.-P. Loock, L. M. Beaty, and B. Simard, Reassessment of the first ionization potentials of copper, silver, and gold, Phys. Rev. A **59**, 873 (1999).

[33] J. C. Pickering and V. Zilio, New accurate data for the spectrum of neutral silver, Eur. Phys. J. D **13**, 181 (2001).

[34] M. K. Nayak, R. K. Chaudhuri, S. Chattopadhyay, and U. S. Mahapatra, Applications of core-valence extensive multi-reference coupled cluster theory and core-extensive coupled cluster-based linear response theory, J. Mol. Struct. Theochem **768**, 133 (2006).

[35] R. K. Chaudhuri and S. Chattopadhyay, Theoretical investigations of electronic spectra of silver atom using all-electron scalar relativistic basis, AIP Adv. **12**, 125019 (2022).

[36] V. A. Dzuba, S. O. Allehabi, V. V. Flambaum, J. Li, and S. Schiller, Time keeping and searching for new physics using metastable states of Cu, Ag, and Au, Phys. Rev. A **103**, 022822 (2021).

[37] W. R. Johnson and G. Soff, The Lamb shift in hydrogen-like atoms, $1 \leqslant z \leqslant 110$, At. Data Nucl. Data Tables **33**, 405 (1985).

[38] B. K. Sahoo, Conforming the measured lifetimes of the $5d\,^2D_{3/2,5/2}$ states in Cs with theory, Phys. Rev. A **93**, 022503 (2016).

[39] J. Cizek and J. Paldus, Coupled cluster approach, Phys. Scr. **21**, 251 (1980).

[40] I. Lindgren, J. Morrison, and F. A. Matsen, Atomic many-body theory, Phys. Today **36**, 82 (1983).

[41] D. Mukherjee and S. Pal, Use of cluster expansion methods in the open-shell correlation problem, Adv. Quantum Chem. **20**, 291 (1989).

[42] K. Kozioł and G. A. Aucar, QED effects on individual atomic orbital energies, J. Chem. Phys. **148**, 134101 (2018).

[43] J. C. Berengut, V. A. Dzuba, and V. V. Flambaum, Isotope-shift calculations for atoms with one valence electron, Phys. Rev. A **68**, 022502 (2003).

[44] M. Kowalska, Ground state properties of neutron-rich Mg isotopes: The "island of inversion" studied with laser and beta-NMR spectroscopy, Mainz University (unpublished).

[45] G. Torbohm, B. Fricke, and A. Rosén, State-dependent volume isotope shifts of low-lying states of group-IIa and -IIb elements, Phys. Rev. A **31**, 2038 (1985).

[46] C. W. P. Palmer, Reformulation of the theory of the mass shift, J. Phys. B: At. Mol. Phys. **20**, 5987 (1987).

[47] M. Doppelbauer, S. C. Wright, S. Hofsäss, B. G. Sartakov, G. Meijer, and S. Truppe, Hyperfine-resolved optical spectroscopy of the $A^2\Pi \leftarrow X^2\Sigma^+$ transition in MgF, J. Chem. Phys. **156**, 134301 (2022).

[48] S. Hofsäss, J. E. Padilla-Castillo, S. C. Wright, S. Kray, R. Thomas, B. G. Sartakov, B. Ohayon, G. Meijer, and S. Truppe, High-resolution isotope-shift spectroscopy of Cd I, Phys. Rev. Res. **5**, 013043 (2023).

[49] D. Röser, J. E. Padilla-Castillo, B. Ohayon, R. Thomas, S. Truppe, G. Meijer, S. Stellmer, and S. C. Wright, Hyperfine structure and isotope shifts of the $(4s^2)^1S_0 \rightarrow (4s4p)^1P_1$ transition in atomic zinc, Phys. Rev. A **109**, 012806 (2024).

[50] R. C. Brown, S. Wu, J. V. Porto, C. J. Sansonetti, C. E. Simien, S. M. Brewer, J. N. Tan, and J. D. Gillaspy, Quantum interference and light polarization effects in unresolvable atomic lines:

Application to a precise measurement of the ^{6,7}Li D_2 lines, Phys. Rev. A **87**, 032504 (2013).

[51] J. Carlsson, P. Jönsson, and L. Sturesson, Accurate time-resolved laser spectroscopy on silver atoms, Z. Phys. D **16**, 87 (1990).

[52] G. Wessel and H. Lew, Hyperfine structures of silver and gold by the atomic beam magnetic resonance method, Phys. Rev. **92**, 641 (1953).

[53] H. Dahmen and S. Penselin, Measurement of the nuclear magnetic dipole moment of Au^{197} and hyperfine structure measurements in the ground states of Au^{197}, Ag^{107}, Ag^{109} and K^{39}, Z. Phys. **200**, 456 (1967).

[54] G. Uhlenberg, J. Dirscherl, and H. Walther, Magneto-optical trapping of silver atoms, Phys. Rev. A **62**, 063404 (2000).

[55] N. J. Stone, Table of nuclear magnetic dipole and electric quadrupole moments, At. Data Nucl. Data Tables **90**, 75 (2005).

[56] W. Fischer, H. Hühnermann, and E. Krüger, The hyperfine structure of the transition Ag I, $\lambda = 19372$ Å, Z. Phys. A **216**, 136 (1968).

[57] T. Badr, M. D. Plimmer, P. Juncar, M. E. Himbert, J. D. Silver, and G. D. Rovera, Continuous-wave Doppler-free two-photon spectroscopy of the SD transition in atomic silver, Eur. Phys. J. D **31**, 3 (2004).

[58] M. Elbel and W. Fischer, Zur Isotopieverschiebung im Silber I- und II-Spektrum, J. Phys. **166**, 504 (1962).

[59] T. Badr, S. Guérandel, M. D. Plimmer, P. Juncar, and M. E. Himbert, Improved frequency measurement and isotope shift of the $4d^9 5s^2\,^2D_{5/2} \rightarrow 4d^{10} 6p^2 P_{3/2}$ transition in silver by laser heterodyne spectroscopy, Eur. Phys. J. D **14**, 39 (2001).

[60] T. Badr, M. D. Plimmer, P. Juncar, M. E. Himbert, Y. Louyer, and D. J. E. Knight, Observation by two-photon laser spectroscopy of the $4d^{10} 5s\,^2S_{1/2} \rightarrow 4d^9 5s^2\,^2D_{5/2}$ clock transition in atomic silver, Phys. Rev. A **74**, 062509 (2006).

[61] I. Angeli and K. P. Marinova, Table of experimental nuclear ground state charge radii: An update, At. Data Nucl. Data Tables **99**, 69 (2013).

[62] J. P. Santos, F. Parente, S. Boucard, P. Indelicato, and J. P. Desclaux, X-ray energies of circular transitions and electron screening in kaonic atoms, Phys. Rev. A **71**, 032501 (2005).

[63] P. Indelicato, Nonperturbative evaluation of some QED contributions to the muonic hydrogen $n = 2$ Lamb shift and hyperfine structure, Phys. Rev. A **87**, 022501 (2013).

[64] M. Trassinelli, D. F. Anagnostopoulos, G. Borchert, A. Dax, J.-P. Egger, D. Gotta, M. Hennebach, P. Indelicato, Y.-W. Liu, B. Manil *et al.*, Measurement of the charged pion mass using x-ray spectroscopy of exotic atoms, Phys. Lett. B **759**, 583 (2016).

[65] N. Michel, N. S. Oreshkina, and C. H. Keitel, Theoretical prediction of the fine and hyperfine structure of heavy muonic atoms, Phys. Rev. A **96**, 032510 (2017).

[66] A. Antognini, S. Bacca, A. Fleischmann, L. Gastaldo, F. Hagelstein, P. Indelicato, A. Knecht, V. Lensky, B. Ohayon, V. Pascalutsa, N. Paul, R. Pohl, and F. Wauters, Muonic-atom spectroscopy and impact on nuclear structure and precision QED theory, arXiv:2210.16929.

[67] N. S. Oreshkina, Self-energy correction to the energy levels of heavy muonic atoms, Phys. Rev. Res. **4**, L042040 (2022).

[68] I. A. Valuev, G. Colò, X. Roca-Maza, C. H. Keitel, and N. S. Oreshkina, Evidence against nuclear polarization as source of fine-structure anomalies in muonic atoms, Phys. Rev. Lett. **128**, 203001 (2022).

[69] I. A. Valuev and N. S. Oreshkina, Full leading-order nuclear polarization in highly charged ions, Phys. Rev. A **109**, 042811 (2024).

[70] J. Bauche, Hartree-Fock evaluations of specific-mass isotope shifts, J. Phys. France **35**, 19 (1974).

[71] Z. Ge, M. Reponen, T. Eronen, B. S. Hu, M. Kortelainen, A. Kankainen, I. D. Moore, D. A. Nesterenko, C. X. Yuan, O. Beliuskina *et al.*, High-precision mass measurements of neutron deficient silver isotopes probe the robustness of the $n = 50$ shell closure, arXiv:2401.07976.